AIAA JOURNAL
Vol. 45, No. 8, August 2007

Wake Vortex Alleviation Using Rapidly Actuated Segmented Gurney Flaps

Claude G. Matalanis* and John K. Eaton†
Stanford University, Stanford, California 94305

DOI: 10.2514/1.28319

A study to assess the potential for using rapidly actuated segmented Gurney flaps, also known as miniature trailing-edge effectors, for active wake vortex alleviation is conducted. Experiments are performed using a half-span model wing with NACA 0012 shape and an aspect ratio of 4.1. The wing is at an 8.9-deg angle of attack and the chord-based Reynolds number is around 350,000. It is equipped with an array of miniature trailing-edge effectors that extend 0.015 chord lengths perpendicular to the freestream on the pressure side of the wing when deployed and sit just behind the blunt trailing edge when retracted. Measurements of section lift coefficient and the velocity field in the intermediate wake using dynamic particle image velocimetry and a five-hole probe delineate the time-varying perturbation imparted by the miniature trailing-edge effectors upon the trailing vortex while keeping the lift nearly constant. The data are used to form a complete initial condition for a vortex filament computation of the far-wake evolution. Cases at the model-scale and full-scale configurations are computed. The results show that actuator-induced perturbations can be used to excite a variety of inviscid vortex instabilities.

Nomenclature

A	=	tangential velocity correction constant
AR	=	wing aspect ratio, $2a/c$
a	=	wing half-span
a_{down}	=	spanwise length of miniature trailing-edge effectors in the down position
b	=	wing span, $2a$
b'	=	vortex spanwise separation
C	=	streamwise velocity correction constant
C_{l_0}	=	section lift coefficient at root
c	=	wing chord length
d_{cut}	=	filament cutoff distance
G_{YY}	=	power spectrum of the spanwise vortex center location with respect to the streamwise length
r	=	radial distance from the vortex center
T_{link}	=	time at vortex close approach
t	=	time
t_{flow}	=	flow timescale, $t_{\text{flow}} = c/U_\infty$
t^*	=	nondimensional time, $t^* = t/t_{\text{flow}}$
U_∞	=	freestream velocity
V_θ	=	tangential velocity
X, Y, Z	=	streamwise, spanwise, and lift coordinates
Y_{flap}	=	spanwise location of the centroid of miniature trailing-edge effectors in the down position
Δt^*	=	nondimensional actuation time
δ_Δ	=	peak-to-peak displacement measure
λ	=	streamwise wavelength
Γ	=	circulation
τ	=	nondimensional time, $\tau = \Gamma_{ell} \Big/ \left(2\pi b_{ell}'^2\right)$

I. Introduction

THE wake vortex hazard continues to be an obstacle in increasing airport capacity. Large, high-lift aircraft create strong vortices in their wake that can persist for long times after the aircraft has passed. To protect following aircraft from the dangers associated with encountering these vortices, airports adhere to spacing rules that restrict the minimum distance between departing aircraft. These rules are becoming more impractical, and the need for other solutions is growing as air traffic increases.

Wake alleviation is a potential solution wherein we somehow render the wake of a large aircraft safe to a following aircraft in less time than would normally be required, thus allowing for a reduction in the minimum required distance between them. A variety of strategies for doing this has been explored over the years, including both passive and active control of wake vortices [1,2]. With active flow control strategies, the idea is to embed time-varying perturbations in the wake that will excite instabilities in the trailing vortex system. The lift experienced by the aircraft must be held nearly constant for this strategy to be practical.

Crow and Bate [3,4] proposed a simple way of doing this to excite the instability that bears Crow's name. The idea involved periodically oscillating the lateral control surfaces on an aircraft such that the total lift would be kept constant, but the loading distribution would vary in time, moving a fraction of the lift periodically inboard and outboard. Bilanin and Widnall [5] and Barber and Tymczyszyn [6] conducted studies based on this idea as well.

More recently, the work of Fabre et al. [7,8], Crouch et al. [9], and Rennich and Lele [10,11], has suggested that even small perturbations of this sort can be applied in a way that can excite vortex instabilities. Rennich and Lele [10] showed that for a four-vortex configuration with the inboard pair counter-rotating with respect to the outboard pair, it is possible to excite an accelerated instability on the system that quickly leads to linking of the strong outboard pair. They conducted vortex filament and Navier–Stokes simulations and showed that only a very small perturbation was necessary to achieve this. The perturbation used in their work was a sinusoidal variation in time, for which the frequency was set near the value that would produce a streamwise wavelength close to the most unstable Crow mode. The decreases in linking time reported were substantial. Considering the same configuration, Fabre et al. [7] examined this instability, as well as other modes, and provided a more complete parametric study.

Crouch [12] extended the stability analysis of Crow to a more general vortex system consisting of four vortices in which the inboard pair are corotating with respect to the outboard pair. The analysis indicated the existence of both long- and short-wavelength instabilities on this system and the possibility of transient growth to initially amplify the instability. Crouch et. al. [9] later showed with

Received 12 October 2006; revision received 5 April 2007; accepted for publication 6 April 2007.

*Graduate Student, Mechanical Engineering, Building 500-501R. Student Member AIAA.

†Professor, Mechanical Engineering, Building 500-501F. Senior Member AIAA.

Navier–Stokes computations and tow tank experiments that a symmetric long-wavelength instability could be excited using small oscillations of conventional control surfaces. Significant decreases in linking time were reported.

The purpose of this work is to assess the potential of miniature trailing-edge effectors (MiTEs) for use in wake alleviation through exciting vortex instability. MiTEs are segmented, rapidly actuated, independent Gurney flaps that affect the aerodynamic characteristics of a wing in the same way that Gurney flaps do, but local to their spanwise position. Each MiTE has a small flap oriented perpendicular to the freestream at the trailing edge, which can increase the section lift coefficient considerably with only a small drag penalty. The flow mechanism responsible for the lift increments on Gurney flaps has been researched extensively [13–20], and recent research has shown that the same mechanism is responsible for the effectiveness of MiTEs [21].

The effect of MiTEs is not limited to the flow immediately surrounding the wing, but can extend into the intermediate wake downstream of the wing. Matalanis and Eaton [22] showed that it is possible to displace the steady-state center of the trailing vortex in both the spanwise and lift directions by actuating MiTEs comprising 13% of the half-span of a wing near its tip. The displacement of the vortex from its nominal location tends to grow as we move further downstream, which indicates that the MiTEs are not changing the origin of the vortex, but rather how the vortex has rolled up as it approaches the intermediate wake. At $X/c = 4.9$, beyond the point at which the vortex is essentially rolled up, the maximum displacements of the vortex center were $4.1\%c$ in the spanwise direction and $1.6\%c$ in the lift direction. These displacements were achieved with a maximum change in total lift of 0.91%. If these displacements can be cycled in time at an appropriate frequency, periodic oscillations can be introduced into the wake that may excite instabilities in the vortex system.

The experiment performed provides data on the transient response of a trailing vortex to MiTE actuation schemes that nearly conserve total lift. A key feature of the MiTEs over conventional control surfaces is that they can be rapidly actuated, allowing us to explore both long- and short-wavelength instabilities. This work includes complementary experimental and computational aspects. Time-resolved velocity field measurements were performed to determine the transient response of the trailing vortex to rapid actuation of the MiTEs. These experimental measurements extended into the intermediate wake, $X/c = 4.9$. The measured time-dependent displacements of the vortex, along with other flow measurements, are used to formulate an initial condition for a vortex filament computation of the far-wake evolution. These computations provide an estimate of how the far wake may evolve due to the perturbations created by MiTEs.

II. Experimental Apparatus

A. Wing and MiTEs

The experimental apparatus consists of a half-span model with NACA 0012 shape. The chord length $c = 300$ mm, half-span $a = 619$ mm, and aspect ratio $AR = 4.1$. The trailing edge of the wing is blunt with $0.02c$ thickness, and the tip is rounded according to the thickness of the wing. All tests were conducted at a chord-based Reynolds number of 350,000 and with the wing at an 8.9-deg angle of attack. The solid blockage ratio in this configuration is roughly 7%. The coordinate system denoted by X, Y, and Z is measured from an origin fixed at the location of the root trailing edge of the wing when the wing is at a 0-deg angle of attack (shown in Fig. 1). Other aspects of the wing design and construction can be found in [22].

The wing is equipped with an array of 26 MiTEs evenly spaced from $Y/a = 0.054$ to $Y/a = 0.919$. Each MiTE is $0.03a$ in span and $0.077c$ in streamwise length, and each has a flap that extends $0.015c$ perpendicular to the flow on the pressure side of the wing. There is a spanwise gap of $0.004a$ between the edges of adjacent MiTE flaps. In this paper, we examine only configurations with zero or four MiTEs down at any time ($a_{\text{down}}/a = 0.0$ or 0.13), and only MiTEs near the tip are actuated ($0.654 < Y_{\text{flap}}/a < 0.854$); this choice is explained in Sec. IV.

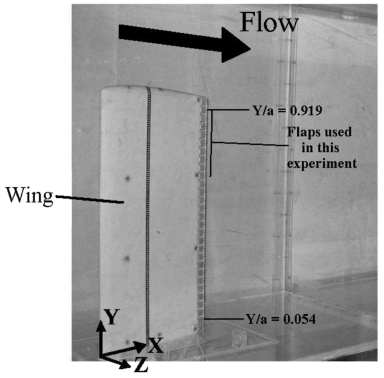

Fig. 1 Wing and MiTEs mounted in the tunnel test section.

Figure 2 shows a picture of a MiTE detached from the wing and oriented in the X–Z plane in both the neutral and down positions. The body of the MiTE is machined out of acrylic and the flap and arm are made out of Delrin machined by laser ablation. The connecting plug in front of the MiTE body is used to transmit current to the dc motor that moves the flap. Steel pins are used as stops to limit the motion of the flap.

The MiTEs are commanded by a computer that sends signals to a circuit that relays a constant voltage signal from a power supply to the desired MiTEs. In Fig. 3, we show the mechanical response of the MiTEs, which is measured with a strobe light and charge-coupled device (CCD) camera. Here, we average the locations of the four flaps closest to the tip at each time point, with the maximum variation amongst the four being less than 20% of the actuation height. Clearly, the motion is underdamped. In moving from one position to the other, the flap quickly accelerates then strikes the metal stop at high speed, causing it bounce off of the metal stop several times before coming to rest. All attempts made to dampen this motion resulted in a loss of consistent behavior between MiTEs and either a very slow actuation time or only a marginal increase in damping. As shown in Fig. 3, the shortest timescales present in the response are roughly $1.0t_{\text{flow}}$ ($t_{\text{flow}} = c/U_\infty$), whereas the timescale based on the response envelope is around three to four times t_{flow}.

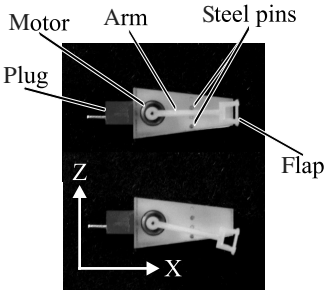

Fig. 2 One MiTE detached from wing and shown in the neutral and down position.

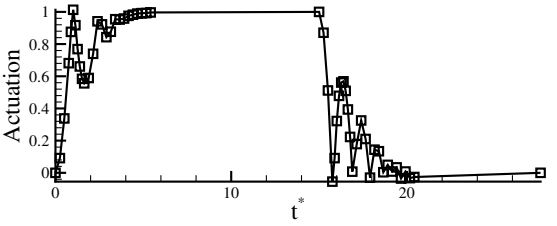

Fig. 3 Mechanical response of the four flaps closest to the tip.

B. Measurement Apparatus

All experiments are conducted in the Stanford Flow Control Wind Tunnel, which is a closed-loop tunnel that operates at atmospheric conditions with a maximum velocity of 22 m/s. The test section is 91 cm high, 61 cm wide, and 3.7 m long. The wing, as shown in Fig. 1, is mounted directly onto the bottom wall of the tunnel (no splitter plate), with the leading edge roughly 45 cm past the beginning of the test section.

Measurement of the section lift coefficient at the root, C_{l_0}, is achieved by a row of pressure taps, each of which is 0.64 mm in diameter, placed along the pressure and suction sides of the wing at $Y/a = 0.081$. This allows us to calculate the circulation at the root of the wing, Γ_0, directly.

Velocity measurements are performed in the intermediate wake ($2.8 < X/c < 4.9$) using particle image velocimetry (PIV) to obtain phase-averaged high-resolution data in the vortex core (primarily to locate the vortex center) and five-hole probe measurements to obtain static low-resolution data over a large domain. The flow is seeded using a glycerin-based fog generator and illuminated with a dual-head Nd:YAG laser capable of 400 mJ/pulse. The laser sheet is oriented perpendicular to the freestream, and the sheet thickness is 2.5 mm. Image pairs are captured using a CCD camera mounted inside the wind tunnel. Interference effects are negligible, as documented in [22]. Cross-correlation PIV is used to process the images and calculate the tangential velocities of the trailing vortex. The velocity field resolution is roughly 0.7 mm. For each velocity field, the vortex center is calculated by finding the location of minimum tangential velocity.

Each actuation scheme consists of two static MiTE configurations. For all dynamic PIV measurements, the MiTEs are actuated periodically between configurations 1 and 2. Typically, the period is set to one second. We are only interested in the transient flow response as the MiTEs move from one configuration to the other, thus the actual period is unimportant. It is selected to insure that all transients had died out and for experimental convenience. Phase-locked PIV sampling is used to resolve the coherent flow response to MiTE actuation without the need for a high-speed PIV system. A timing diagram for measuring the transient response going from configuration 1 to configuration 2 is shown in Fig. 4. The MiTEs are initially in configuration 1, then at time $t^* = 0$, they are commanded to move to configuration 2. At nondimensional time t^*, the computer triggers the PIV system to acquire an image pair. The nondimensional time t^* ranges from $0 < t^* < 10$ in intervals of 0.32. The time between the two laser pulses required for a single PIV velocity field measurement was 20 μs ($0.0013 t_{\text{flow}}$). This interimage separation time was insignificant relative to the t^* interval. A set of 200 image pairs is acquired for each set value of t^*, and the 200 instantaneous velocity fields are averaged to give the phase-averaged velocity field. This process was repeated for a minimum of 18 different values of t^* for the actuation of the MiTEs from configuration 1 to configuration 2, and an additional minimum of 18 values of t^* for the actuation from configuration 2 to configuration 1. Measurements are taken at three positions behind the wing, $X/c = 2.8, 3.8$, and 4.9. According to the estimates given by Spreiter and Sacks [23], the vortex should be fully rolled up at a distance $X/c = 2.75$.

Steady-state velocity measurements are performed at the $X/c = 4.9$ streamwise location using a five-hole probe. Three components of velocity are measured over a square region 20 by 20 cm large using a two-component (Y, Z) traverse mounted on top of the tunnel test section.

All other aspects of the experimental procedures and uncertainty analysis are identical to those reported in [22]. In the following, the critical experimental results needed as input to the computational study are the vortex center location and the wing root circulation. These are derived from the detailed PIV measurements and the pressure distribution, respectively. The most conservative uncertainty estimate for the vortex center location proved to be the repeatability of the measurement, which is $\pm 0.001c$. This is likely due to several very small sources of error that cannot be quantified. The uncertainty in wing circulation, Γ_0, accounting for statistical uncertainty, transducer drift, uncertainty in angle of attack, and uncertainty in freestream velocity, is ± 0.013 m^2/s.

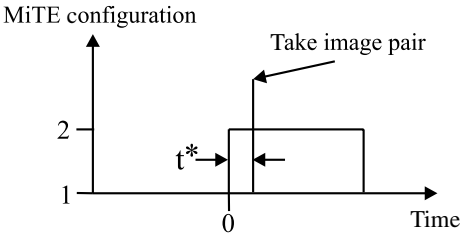

Fig. 4 Order of events for collecting one dynamic PIV sample going from configuration 1 to configuration 2.

III. Computational Approach

The data collected in the intermediate wake are used to form a complete initial condition for a computation of the far-wake evolution. The work of Rennich and Lele [10] showed that instability amplification rates could be predicted fairly accurately (errors less than 10%) if the wake data are taken far enough downstream that the vorticity is essentially rolled up. This is the case in the present experiment. Crouch et al. [9] provides further confirmation of this. We consider a stationary reference frame in which the flow is initially quiescent until the aircraft or wing moves through it at velocity U_∞. Applying Taylor's hypothesis, changes in the vortex center location with respect to time in the frame of the moving wing become changes with respect to streamwise distance in the stationary frame. We assume that the time taken by the aircraft to traverse the domain is much smaller than the time that will be required for any instability on the vortices to grow. Thus, the flow can be treated as periodic in the streamwise direction.

The vortex filament technique has been used extensively to model vorticity dominated flows [24,25]. It is well suited for this application because the computed flow is governed mostly by vorticity concentrated along the locations of the trailing vortices. The lack of an Eulerian grid provides relatively fast computations that allow us to analyze many cases and explore large parameter ranges. This technique affords very good predictions of initial growth rates and fair predictions at intermediate times. However, the method becomes less accurate as two vortices closely approach one another or the curvature of an individual vortex becomes too high. Rennich and Lele [10] compared vortex filament calculations to Navier–Stokes results for pure Crow instability. They showed that for calculations involving two vortices, the filament technique tends to underpredict growth rates at later times, thus providing a conservative approximation of linking time. We used the same code as Rennich and Lele, and all computations are terminated whenever a filament comes within two cutoff distances of itself or another filament. The time at which this occurs is designated T_{link}, however, vortex linking is a highly viscous process that cannot be modeled properly with a computation of this sort. Thus, the relationship between T_{link} as we define it and the actual vortex linking time are not known; however, the parameter T_{link} provides us with a rough estimate of linking time and is a good parameter for fair comparison between the various cases examined below.

The present far-wake vortex filament computations cannot replace high-accuracy Navier–Stokes computations, well-designed far-wake experiments, or actual flight testing. We use this technique only to provide us with a reasonably likely scenario of how the far wake may evolve given the clearly stated assumptions.

The vortex filament code was developed at Stanford University and is described in detail by Rennich and Lele [10]. This is an inviscid incompressible code wherein each vortex is represented by one smooth, continuous filament. Each filament is defined by a set of nodes in three dimensions that are connected by cubic spline elements. The induced velocity at each node is computed by performing the Biot–Savart integral along all filaments in the domain. The code uses fifth-order-accurate Gaussian quadrature for

integration and fourth-order Runge–Kutta time advancement. The periodic boundary condition in the streamwise direction is enforced using ghost filaments.

The cutoff technique is used to remove the singularity in the Biot–Savart law and to model the vorticity distribution of the vortex. This approach is discussed in detail in [3,26]. The cutoff distance d_{cut} is chosen using the relation

$$\ell_n \frac{d_{\text{cut}}}{b'} = -\ell_n 2 + \frac{1}{2} - A + C \tag{1}$$

where A and C are corrections to account for tangential and streamwise velocities, respectively, and are given by the relations

$$A = \lim_{r\to\infty}\left(\frac{4\pi^2}{\Gamma^2}\int_0^r r^* V_\theta^2 \mathrm{d}r^* - \ell_n \frac{r}{b'}\right) \tag{2}$$

$$C = \lim_{r\to\infty}\left(\frac{4\pi^2}{\Gamma^2}\int_0^r 2r^* U^2 \mathrm{d}r^*\right) \tag{3}$$

where r is the radial distance from the vortex center, V_θ is the tangential velocity, and Γ is the total circulation in the vortex. The velocity field is measured over a large domain in the experiment using a five-hole probe. The limits going to infinity make it impossible to evaluate A and C exactly from the five-hole probe measurements, due to the finite measurement domain. They can be reasonably approximated by maximizing the r value at which the integrals in Eqs. (2) and (3) are evaluated. Figure 5 shows a plot of d_{cut} as a function of the radial extent of the integration domain. The curve shown is an ensemble average compiled using five-hole probe profiles from all of the MiTE configurations used in the active schemes. The change in this curve due to changing MiTE configurations is small (± 0.002 in d_{cut}/b'). Clearly, d_{cut} has not completely converged. We examine the sensitivity of T_{link} to variations in d_{cut} and λ in a parametric study shown in Fig. 6. The initial perturbation shapes used here are sinusoidal, and the vortex configuration is identical to that of our model case, which will be discussed later. There is clearly a weak dependence of T_{link} upon d_{cut}. Furthermore, slight modifications in λ could eliminate any difference. Thus, we take the value of d_{cut} to be the largest measured value from Fig. 5, $d_{\text{cut}}/b' = 0.0332$; this nondimensional value is used for all computations.

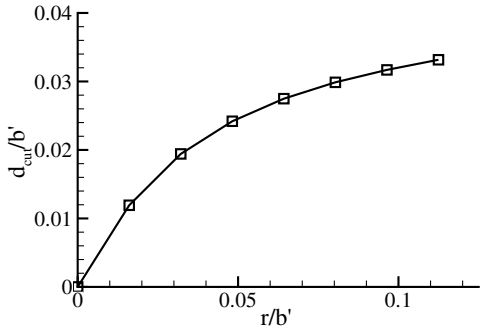

Fig. 5 Relationship between cutoff length and chosen domain size.

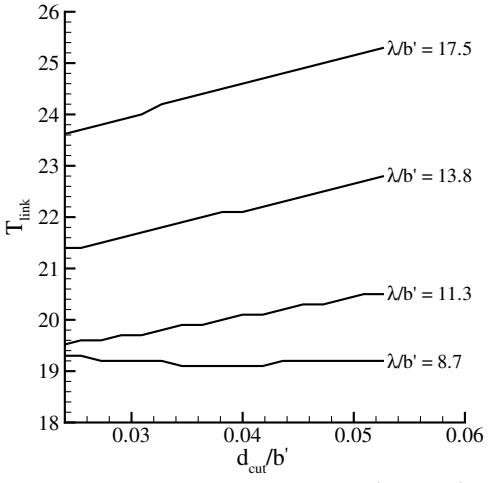

Fig. 6 Parametric study on the influence of d_{cut}/b' and λ/b' upon T_{link}.

The strength of the vortex is taken from a measurement of C_{l_0}, the section lift coefficient at a spanwise station very close to the root ($Y/a = 0.081$). The vortex circulation Γ is related to C_{l_0} by $\Gamma = (1/2)C_{l_0}U_\infty c$, which comes from lifting line theory. The effect upon C_{l_0} of the flap configurations examined is very small, thus Γ is left constant along the filament. Several trial cases were run that demonstrated that varying Γ along the filament tends to reduce T_{link}, thus leaving Γ constant is more conservative.

Time and filament refinement studies using sinusoidal perturbation shapes were performed to insure that sufficiently fine time steps and nodal spacing are used. All cases in this work were run using $(\Delta t\Gamma)/(2\pi b'^2) < 0.04$ and $(\Delta x)/(b') < 0.2$, where Δt is the dimensional time step, and Δx is the dimensional initial nodal spacing in the X direction. Further refinements in both time steps and nodal spacing indicated changes in T_{link} of less than 2%.

Finally, all that remains is to establish the initial shape of the filaments. To do this, we determine the vortex center location in the wake and how it responds to the actuation of the MiTEs from our dynamic PIV measurements. Those measurements are presented in the following section.

IV. Intermediate Wake Measurements

A. Active Scheme Design

The steady-state vortex center locations for the neutral case and three static MiTE configurations are shown in Fig. 7. Aside from the neutral case, each configuration has four contiguous flaps in the down position ($a_{\text{down}}/a = 0.13$). The position of the actuated set is defined based on the spanwise center of the four actuated flaps, Y_{flap}, and is normalized by the wing half-span a. For all cases, data are collected at three streamwise positions in the intermediate wake ($X/c = 2.8, 3.8, 4.9$). All of the active schemes consist of cycling between two of the static configurations shown in Fig. 7 (i.e., configurations 1 and 2 for each scheme will be selected only from Fig. 7). We will begin by examining one simple actuation scheme for which configuration 1 is the neutral case and configuration 2 is putting the four flaps closest to the tip in the down position ($a_{\text{down}}/a = 0.13$, $Y_{\text{flap}}/a = 0.854$). This will be primarily to establish a baseline.

Because the goal is to excite vortex instability, the best active scheme will likely be one that maximizes the spanwise displacement experienced by the vortex. It may also be desirable, however, to choose a scheme in which the vortex moves in the spanwise and lift directions to resemble the most unstable eigenmode reported by Crow [3]. Thus, we examine the following active schemes: scheme A

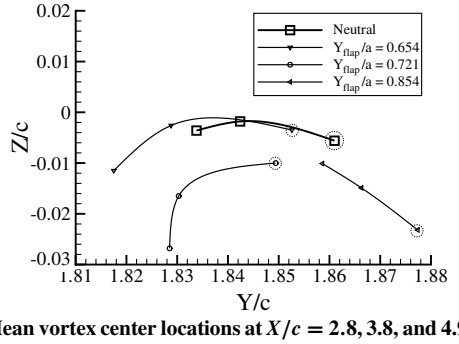

Fig. 7 Mean vortex center locations at $X/c = 2.8, 3.8$, and 4.9 for cases where $a_{\text{down}}/a = 0.13$. The vortex location at $X/c = 2.8$ for each configuration is denoted by a dashed circle and data for $X/c = 3.8$ and 4.9 are connected by lines consecutively. The uncertainty in both directions is indicated by the symbol size of the neutral case.

Table 1 Flap configurations for the three active schemes.

Scheme	Configuration 1	Configuration 2
Simple	Neutral	$Y_{\text{flap}}/a = 0.854$
A	$Y_{\text{flap}}/a = 0.654$	$Y_{\text{flap}}/a = 0.854$
B	$Y_{\text{flap}}/a = 0.721$	$Y_{\text{flap}}/a = 0.854$

has configuration 1 as $Y_{\text{flap}}/a = 0.654$ and configuration 2 as $Y_{\text{flap}}/a = 0.854$, and scheme B has configuration 1 as $Y_{\text{flap}}/a = 0.721$ and configuration 2 as $Y_{\text{flap}}/a = 0.854$; this is summarized in Table 1. Transient data for schemes A and B are examined only at the furthest streamwise location ($X/c = 4.9$), because these data are used to initialize the computations.

B. Vortex Transient Response

For all schemes, we use the same criterion to determine that the vortex has either begun to move or stopped moving. The nearest point to fall outside of the uncertainty ($\pm 0.001c$) with respect to all of the prior or following points is taken to indicate that the vortex has begun or ceased to move, respectively. Thus, a displacement of $0.002c$ is considered significant. We adhere strictly to this criterion to fairly assess vortex response times of the three schemes. Time is nondimensionalized by the flow timescale $t_{\text{flow}} = c/U_\infty$.

The transient response of the vortex to a simple MiTE actuation scheme is first studied to establish a baseline and determine what aspects of the mechanical actuation carry over to the trailing vortex and how they are modified in the process. For this simple scheme, configuration 1 is all MiTEs in the neutral position and configuration 2 is the four MiTEs closest to the tip ($Y_{\text{flap}}/a = 0.854$), in the down position.

The response of the vortex for this scheme going from configuration 1 to configuration 2 is shown in Figs. 8a and 8c, in which we plot the center location of the vortex as a function of t^* at each streamwise location. Essentially every point along the transient path of the vortex lies between the two steady-state locations. Thus, there is no significant overshoot in the motion of the vortex. The nondimensional time t^* necessary for the vortex to get from its initial steady-state location to the next is between 3.5 and 4.2 for this scheme. These times are comparable to the longer timescales found in the mechanical response of the flaps. This suggests that the overall response of the vortex going from one steady-state location to another tends to be quasi-steady.

We turn now to the shorter timescales that are clearly present in both the mechanical and vortex responses, due to the underdamping of the flap mechanism. Early in the flap mechanical response (Fig. 3), the flap receives a signal at $t^* = 0.0$ and moves rapidly from the neutral position to the fully actuated position by $t^* = 1.0$. For a truly quasi-steady vortex response, we would expect that after some time of flight, the vortex would track with the flap and move the entire distance from its initial to its final steady-state location in the same amount of time. What we see, however, is that $1.0t_{\text{flow}}$ after the vortex has started moving (at $t^* = 4.8$ for $X/c = 3.8$ in Fig. 8a, for example), the vortex has only moved roughly half of this distance. There is a slight leveling off in the spanwise motion of the vortex at that time that is probably in response to the bounce in the flap motion, however, the uncertainty in the measurement prevents a definitive conclusion on this. It is clear that the vortex response to the shorter timescales of the mechanical response is not entirely quasi-steady.

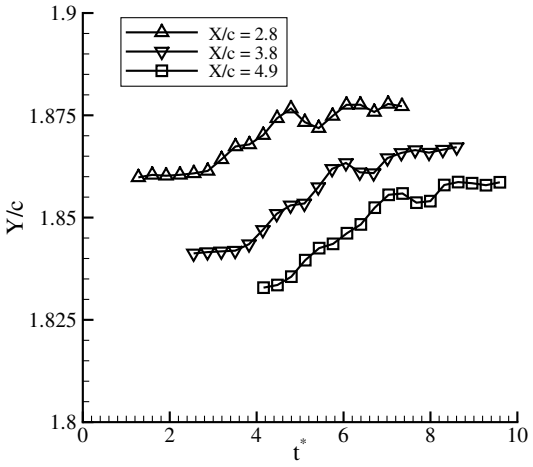

a) Spanwise displacement (configuration 1 to configuration 2)

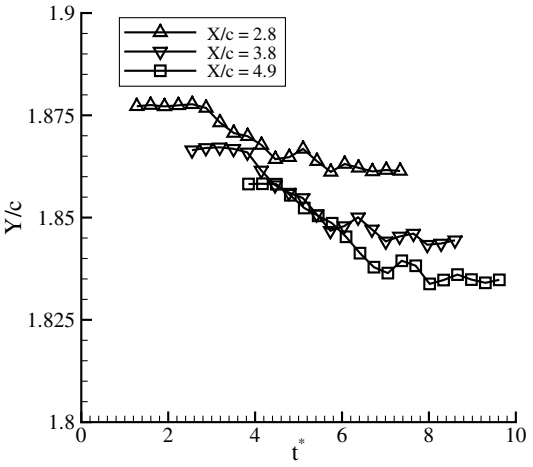

b) Spanwise displacement (configuration 2 to configuration 1)

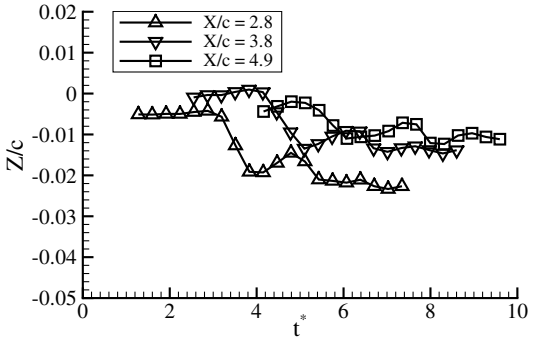

c) Lift direction displacement (configuration 1 to configuration 2)

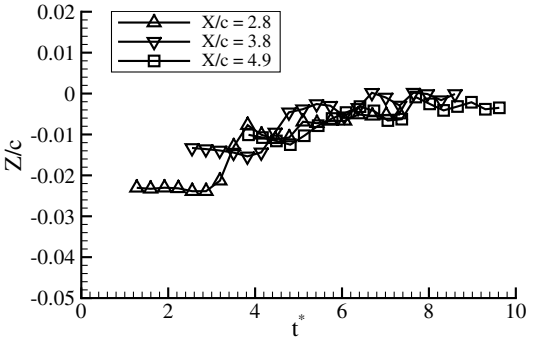

d) Lift direction displacement (configuration 2 to configuration 1)

Fig. 8 Transient response of the vortex center location for the simple MiTE actuation scheme where configuration 1 is the neutral case and configuration 2 is $(Y/a)_{\text{flap}} = 0.854$, $a_{\text{down}}/a = 0.13$. The uncertainty is smaller than the symbol size.

There is a lag time associated with the vortex response when the actuation time is less than or equal to t_{flow}.

The vortex response for this actuation scheme going from configuration 2 to configuration 1 is shown in Figs. 8b and 8d. There are some slight differences in the mechanical response (longer actuation time, different response curve) that cause some slight changes in the vortex response, but all of the same observations made on the previous scheme are apparent in this one as well.

These results are consistent with work done previously regarding dynamic flow response to actuators of this type. Solovitz and Eaton [27] found that for relatively slow actuation times ($\Delta t^* > 1$), the flow response at the trailing edge immediately behind the MiTEs tends to be nearly quasi-steady. This is because several vortices are shed at the trailing edge in the time necessary for the flap to move from one location to another. For faster actuation times ($\Delta t^* < 1$), it was found that the vortex shedding could become phase-locked with the motion of the flap and a significant overshoot in Gurney flap effectiveness was observed. For the trailing vortex, when $\Delta t^* \approx 1$, we do observe a response that is not quasi-steady, however, there is no overshoot. This suggests that the mechanism responsible for transient behavior in the trailing vortex is not the same as that of the immediate flap wake.

Figure 9 shows the vortex response at $X/c = 4.9$ for MiTE actuation schemes A and B that were described in the previous section. These schemes are more complex than the simple scheme discussed previously in that now we have a set of four flaps moving from the neutral to the down position while simultaneously, another four flaps are moving from the down to the neutral position. We begin by examining scheme A, in which the vortex motion is predominantly in the spanwise direction. The nondimensional time required for the vortex to get from configuration 1 to configuration 2 is roughly 4.2 and to get from configuration 2 to configuration 1 is roughly 4.5. Thus, even though the vortex must traverse almost twice as much distance as it did for the simple scheme, the response time is only slightly greater. Considering scheme B, we find that the time necessary for the vortex to get from configuration 1 to configuration 2 is roughly 4.2, and from configuration 2 to configuration 1 is roughly 4.8. Again, these times are only slightly longer than the response times for the simple scheme. This further suggests that the overall motion of the vortex from one steady-state location to the next tends to be quasi-steady, given the mechanical response of these MiTEs. The shorter timescales in the mechanical response affect the path of the vortex, but not the overall response time.

Both the response time of the vortex to MiTE actuation and the path that the vortex takes are critical to determining whether or not exciting vortex instability will be possible. The response time of the vortex puts a finite limit on the shortest perturbation wavelength possible. The fundamental mode wavelength can be arbitrarily increased by going from configuration 1 to configuration 2, then waiting a long time before going back to configuration 1. It cannot be decreased indefinitely due to the finite response time. The path of the vortex governs the shape of the perturbation waveform. The path is never a perfect sinusoid, thus it contains wavelengths other than the predetermined fundamental mode. The measured vortex paths provide us with initial conditions for computations of the far-wake evolution.

V. Far-Wake Computations

The initial conditions of the filaments are established as follows. From the dynamic PIV, the transient motion of the vortex center as a function of time at $X/c = 4.9$ is converted into a spatially varying path using Taylor's hypothesis with the convection velocity taken as U_∞. Thus,

$$(X)_{\text{computations}} = (U_\infty t)_{\text{experiments}} \tag{4}$$

From here on, we refer to $X_{\text{computations}}$ as simply X, aware that we are now in a stationary reference frame. For either actuation scheme A or B, the MiTEs' motion is relatively fast, and so the streamwise distance required for the vortex to move from configuration 1 to configuration 2 or configuration 2 to configuration 1 is always smaller than half of the wavelength of the instability we attempt to excite. Thus, the periodic shape of the filament will consist of going

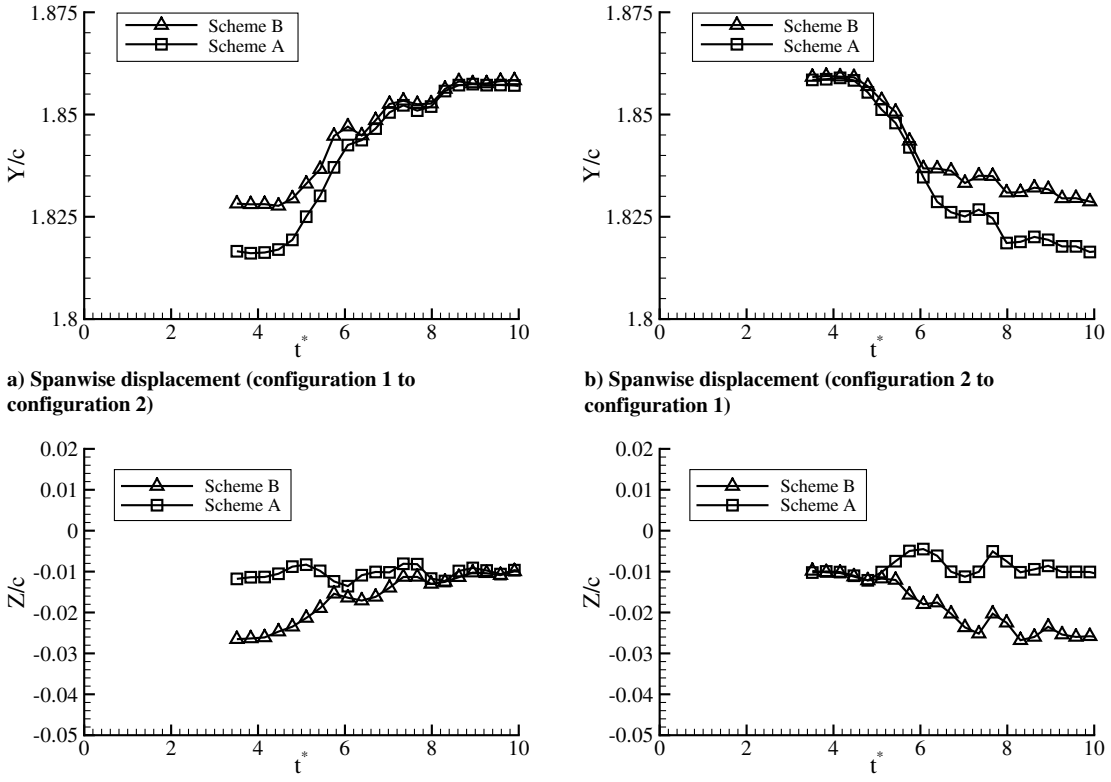

a) Spanwise displacement (configuration 1 to configuration 2)

b) Spanwise displacement (configuration 2 to configuration 1)

c) Lift direction displacement (configuration 1 to configuration 2)

d) Lift direction displacement (configuration 2 to configuration 1)

Fig. 9 Transient response of the vortex center location to MiTE actuation schemes A and B.

from configuration 1 to configuration 2 along the corresponding experimentally determined path, waiting a set time, then moving from configuration 2 to configuration 1 along another experimentally determined path, waiting a set time, and repeating the process. Using Eq. (4), we convert each t^* data point from the dynamic PIV measurements to a node at (X, Y, Z) for configuration 1 to configuration 2 and configuration 2 to configuration 1. To construct just one full period of a filament, connector nodes are added before (configuration 1 to configuration 2), in between (configuration 1 to configuration 2) and (configuration 2 to configuration 1), and after (configuration 2 to configuration 1) generating the desired wavelength. The spacing for these connector nodes is chosen to be as close as possible to the spacing of the data nodes. Finally, the nodal (Y, Z) positions are calculated by linear interpolation from the start and end points of the data nodes while maintaining periodicity of the filament. The X origin is arbitrary. Each vortex is represented with one filament. Initial conditions are generated for two filaments such that they are symmetric with respect to the X–Z plane at $Y = 0$.

Filament computations are run for several vortex configurations. The first case examined is at the model scale, in which all parameters are taken exactly from the experiment. Then we nondimensionalize the experimental parameters and use them to derive three other cases for which the total lift, span, and chord are close to that of a large commercial aircraft. These full-scale cases are performed to examine how perturbations created by the MiTEs might be used to excite other instabilities known to exist on wakes with multiple vortex pairs in a more realistic configuration.

A. Model-Scale Case

All of the computational parameters for the first simulation are taken directly from the experiment and are as follows: $b' = 1.100$ m, $\Gamma = 2.19$ m^2/s, and $\lambda/b' = 9.36$ m. Figure 10 illustrates the initial filament shape created by scheme A, for which the perturbation is mostly in the spanwise direction. Because the perturbation amplitude is small, the Y-axis scale is greatly exaggerated. The streamwise wavelength λ that we choose for this computation is $9.36b'$, which is close to the most unstable wavelength for Crow instability on these filaments. Figure 11 shows plots of the filament shapes in the X–Y and X–Z planes at several times. The most obvious trend is that the vortices move down by mutual induction at a nearly constant velocity. The growth of the Crow instability is apparent after 6.0 s in the spanwise direction. Beyond $t = 12$ s, the instability amplitude grows rapidly until the vortices approach one another too closely at $T_{\text{link}} = 18.0$ s when the computation is terminated.

Despite the presence of shorter wavelengths in the initial filament shape, the evolution of long-wavelength Crow instability is essentially unaffected. Computations run with the same parameters but a pure sinusoidal perturbation rather than the experimentally measured shape were nearly identical. This confirms the expected lack of receptivity of Crow instability to relatively short wavelengths.

The same computation was run using the initial condition given by scheme B, in which the perturbation shape is closer to the most unstable Crow eigenmode but the amplitude is slightly smaller. It was found that T_{link} is slightly shorter for scheme B, but the difference is small and the results were very similar, thus we only present scheme A.

B. Full-Scale Cases

Crow instability tends to exhibit rather slow growth rates when compared with other inviscid instability mechanisms involving two or more pairs of vortices [1,2,9,10,12]. To examine whether or not

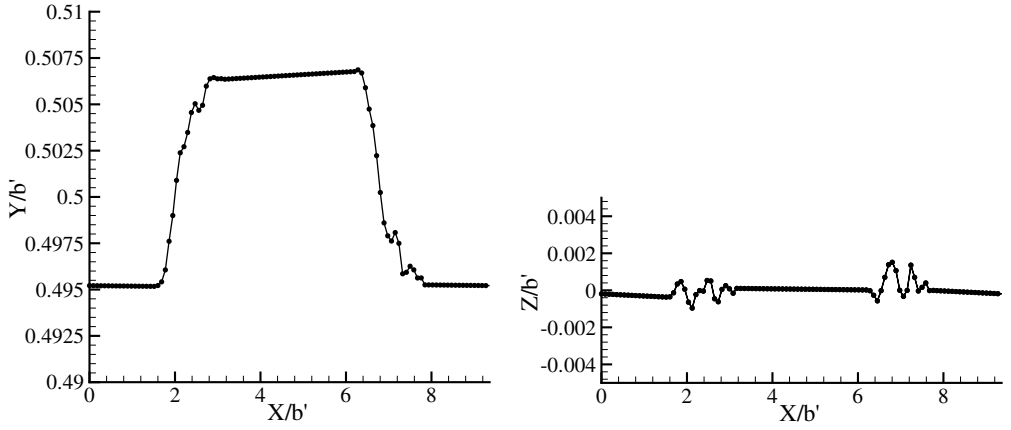

a) Spanwise initial condition **b) Lift direction Initial Condition**

Fig. 10 Initial condition generated from transient response data for scheme A.

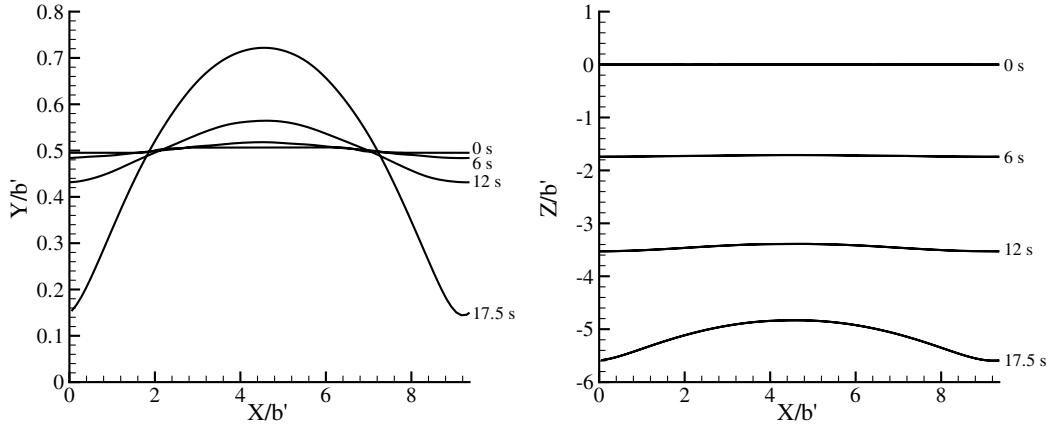

a) Spanwise evolution **b) Lift direction evolution**

Fig. 11 Plots of the filaments for the model-scale case in the X–Y plane at different times.

vortex perturbations created by MiTEs are able to excite other instabilities on a wake that more closely resembles that of a large commercial aircraft, we use our experimental parameters to derive three full-scale vortex configurations.

The measured nondimensional loading distribution was applied to a hypothetical aircraft with a wing span of 66 m, a total lift of 430 tons, and a velocity of 82 m/s. These are reasonable values for a large commercial airliner at takeoff. The perturbation amplitudes in the Y and Z directions are scaled with the vortex separation. To convert the time-varying response of the vortex to a streamwise spatial variation, we evoke the same assumptions used previously, and in addition, we assume that the MiTEs on our hypothetical full-scale configurations are dynamically equivalent, that is,

$$\left(\frac{\Delta t U_\infty}{c}\right)_{\text{experiment}} = \left(\frac{\Delta t U_\infty}{c}\right)_{\text{full scale}} \tag{5}$$

For fair comparison of our results to results with alternative loading distributions, we introduce a nondimensional time variable that is based on an elliptic loading distribution with the same total lift as our three hypothetical cases, $\tau = [\Gamma_{ell}/(2\pi b'_{ell})]t$.

Three hypothetical full-scale vortex configurations are examined: the one-pair configuration (1P), the two-pair corotating configuration (2PCR), and the two-pair counter-rotating configuration (2PCTR). The first is a simple application of the three stated parameters, whereas the other two involve superposing two scalings of our nondimensional loading distribution with different individual spans and lifts that have the same wing span and total lift. These three vortex configurations are shown schematically in Fig. 12, and the loading distributions that would produce them are shown in Fig. 13. The 2PCR case is motivated by the work of Crouch et al. [9], wherein long- and short-wavelength instabilities that evolve faster than pure Crow instability may be excited. The 2PCTR case uses a special loading distribution based on the work of Rennich and Lele [10], wherein we may excite an accelerated long-wavelength instability. The computational parameters for each are given in Table 2. For all hypothetical loading distributions, we perturb only the outboard vortices, thus implying that MiTEs are placed only near the wing tips. We limit our study to symmetric perturbations only. Again, schemes A and B proved to be very similar, with slightly faster

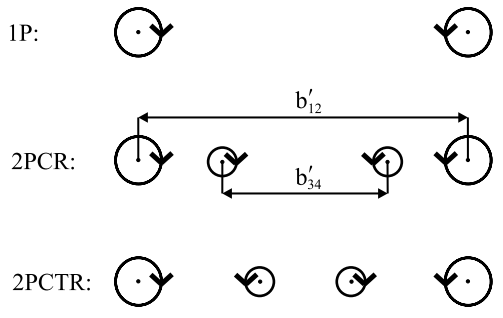

Fig. 12 Diagram of the three vortex configurations examined.

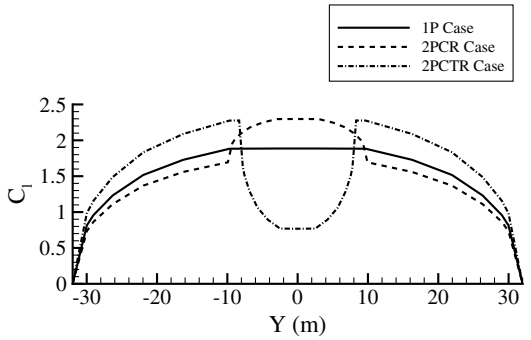

Fig. 13 Spanwise loading distributions required to generate the vortex configurations examined.

Table 2 Computational parameters for the full-scale cases

	b'_{12}, m	b'_{34}, m	Γ_{12}, m^2/s	Γ_{34}, m^2/s	λ/b'_{12}
1P	58.68	N/A	696.0	N/A	9.36
2PCR-long	58.68	18.20	627.8	219.7	6.45
2PCR-short	58.68	18.20	627.8	219.7	2.81
2PCTR	58.68	15.26	841.0	−557.6	9.36

growth rates for scheme B, thus we only present results from scheme A.

For the 1P case, the evolution of Crow instability follows the predicted exponential growth rate and is quite similar to that of the model-scale case. Close approach of the two vortices occurs at $\tau = 6.92$. This gives a baseline for comparison with other full-scale cases.

For the 2PCR configuration, each inboard vortex (vortices 3 and 4) has the same rotationality as its outboard counterpart (vortices 1 and 2); thus, the inboard vortices rotate about the outboard ones as the entire configuration descends regardless of which (if any) instability is growing. The spanwise spacing ratio, circulation ratio, and wavelength (b'_{34}/b'_{12}, Γ_{34}/Γ_{12}, and λ) are set close to the same values used by Crouch et al. [9] and are given in Table 2 (2PCR-long). Figure 14 shows several plots in time of one wavelength of filaments in the X–Y plane. As the weaker vortices (gray) rotate about the stronger vortices (black), the long-wavelength instability grows at the rate predicted by Crouch's analysis until close approach of the two outboard vortices at $\tau = 4.07$. Unfortunately, the MiTE perturbations do not lead to much transient growth; nonetheless, compared with pure Crow instability, we observe a significantly shorter time to close approach. Another important feature of this case is that as this long-wavelength instability grows, the filaments also display a shorter wavelength perturbation, which is apparent in Fig. 14e. This is brought on by the shorter wavelengths present in the initial conditions (due to the fast overall response of the MiTEs), but in this case, they do not affect the evolution of the long-wavelength instability.

The relatively fast motion of the MiTEs (given our assumption of dynamic equivalence) allows us to explore short-wavelength instability (2PCR-short). Setting λ to the short-wavelength symmetric mode described by Crouch [12], we observe a higher initial amplification rate, as expected. Several X–Y plots in time are shown in Fig. 15. Again, the weaker vortices rotate about the stronger vortices as the short-wavelength instability grows. With this instability, however, at $\tau = 2.84$, close approach of the weaker inboard vortices occurs rather than the outboard ones, and it is unknown how the outboard vortices will evolve from there on.

Finally, we attempt to excite the accelerated instability mechanism described by Rennich and Lele [10]. The spanwise spacing and circulation ratios b'_{34}/b'_{12} and Γ_{34}/Γ_{12} are chosen according to the relation given by Rennich and Lele, such that the entire system translates downward rigidly and the vortices are not rotating around one another. The wavelength is set close to the most unstable pure Crow mode for the outboard filaments, $\lambda = 9.36b'_{12}$. The instability, as described by Rennich and Lele, initially involves a long-wavelength perturbation displacing the inboard pair in both the spanwise and lift directions. As the inboard pair becomes deformed, a long-wavelength perturbation on the outboard pair becomes apparent. The perturbation on the outboard pair grows rapidly until the outboard pair links and is destroyed.

When the vortices are initially perturbed using the MiTE perturbation, we see different behavior. Short wavelengths present in the initial condition of the outboard vortices (again, due to the fast overall response of the MiTEs) tend to impart short-wavelength perturbations on the inboard vortices after a small amount of time. As a result, a pure Crow instability grows on the inboard pair and causes them to link before the outboard pair perturbation has grown by very much. This corresponds to the faster-growing instability mode discussed by Fabre et al. [7,8]. Two X–Y plots shown in Fig. 16 illustrate this. To analyze this case more carefully, we examine the time evolution of the power spectrum of spanwise vortex center

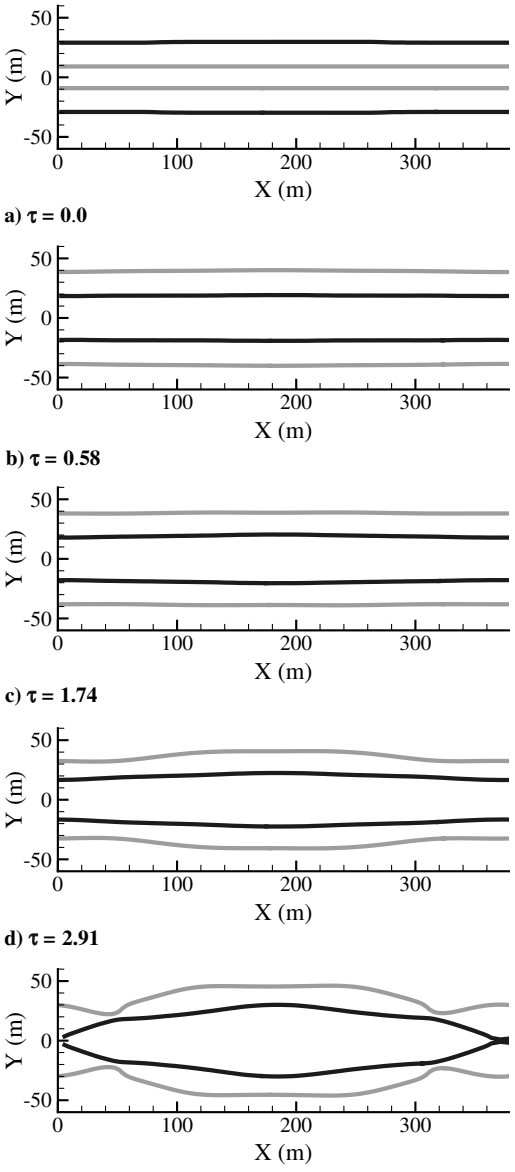

Fig. 14 Plots of the filaments for the 2PCR-long case in the *X–Y* plane. The strong, outboard vortex pair (vortices 1 and 2) is shown in black.

location with respect to streamwise wavelength on the inboard vortices, $G_{YY34}(\lambda)$. This spectrum quantifies the magnitude of perturbations in the spanwise direction that are contained in different streamwise wavelengths of the inboard vortices. We consider two wavelengths: λ_1 corresponds to the long-wavelength perturbation that would eventually lead to linking of the outboard pair, and λ_2 corresponds to the pure Crow instability growing on the inboard pair ($\lambda_1 \approx 9.36 b'_{12}$, $\lambda_2 \approx 12.07 b'_{34}$). The time evolution of the spectrum evaluated at these two wavelengths is shown in Fig. 17. Initially, the long wavelength dominates, but by $\tau = 0.35$, the short-wavelength perturbation has become greater. This leads to close approach of the inboard pair at $\tau = 0.45$ when the computation is terminated.

This receptivity to the shorter wavelengths present in the perturbation highlights the importance in this case of the shape of the perturbation used (i.e., pure sinusoidal perturbations would not have caused this). It is likely that this inboard linking could be avoided by slowing the motion of the MiTEs, but no experimental data on slower-moving MiTEs is available. Attempts were also made to avoid this by modifying the circulation and span ratios of the vortex configuration to slow the growth of the instability on the inboard pair. It was found that lengthening the separation between the inboard pair b'_{34} was somewhat helpful, and this is why the configuration used in this work (given by the values in Table 2) differs from the

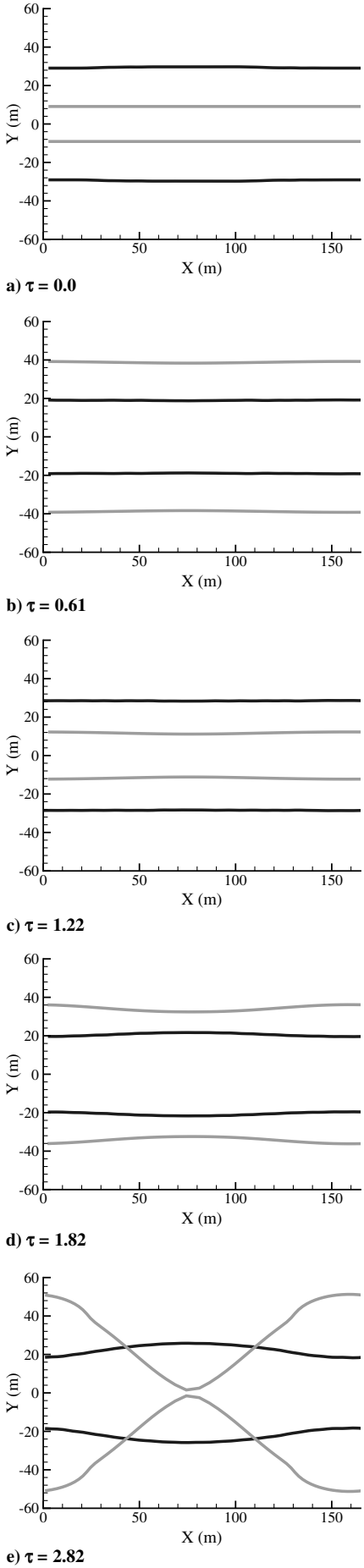

Fig. 15 Plots of the filaments for the 2PCR-short case in the *X–Y* plane. The strong, outboard vortex pair (vortices 1 and 2) is shown in black.

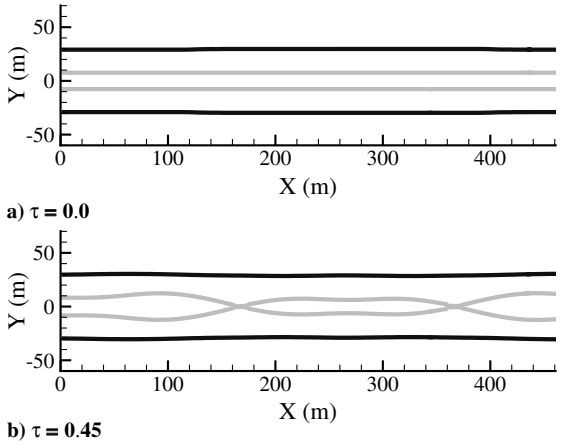

Fig. 16 Plots of the filaments for the 2PCTR case in the X–Y plane. The strong, outboard vortex pair (vortices 1 and 2) is shown in black.

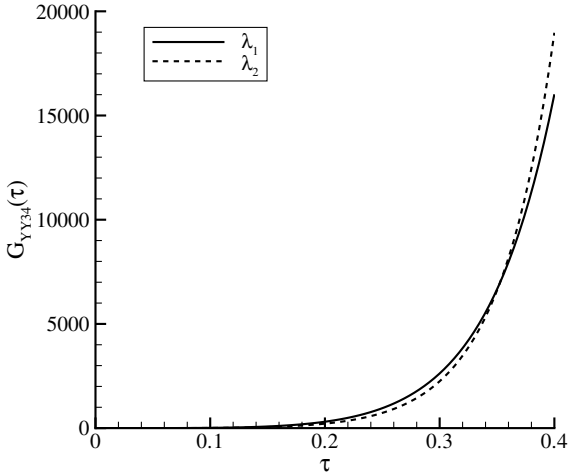

Fig. 17 Time evolution of the spanwise power spectrum at two wavelengths ($\lambda_1 \approx 9.36b_{12}$, $\lambda_2 \approx 12.07b_{34}$) for the 2PCTR case.

configuration chosen by Rennich and Lele [10]. No modification to this configuration was found that would prevent the premature inboard linking, however, a rigorous parametric study was not conducted because it is beyond the scope of this work.

Figure 18 summarizes the evolution of each instability mechanism that we have attempted to excite. Here, we plot the nondimensional displacement measure δ_Δ/b' of one outboard vortex as a function of τ. This displacement measure is simply the maximum peak-to-peak displacement of the vortex center projected on the Y–Z plane, a good measure of how perturbed a vortex has become. As indicated in the figure, the 1P and 2PCR-long cases are terminated upon close approach of the stronger outboard vortices, whereas the 2PCR-short and the 2PCTR cases are terminated upon close approach of the inboard vortices. Because the parameter τ is based on an elliptic loading distribution of the same total lift as our three cases, we can compare these results to that of actual aircraft. For a Boeing 747-400 in calm atmospheric conditions, vortices can persist beyond $\tau = 5.4$ [9]. The 2PCR-long case clearly shows improvement over this. For the 2PCR-short and 2PCTR cases, if we assume that after the inboard pair linking occurs, the outboard pair proceeds to evolve at the slow pure Crow rate (a conservative assumption), then there is still some improvement. It is possible that after the inboard pairs link up, the instability on the outboard vortices will continue to grow faster than pure Crow because whatever remains of inboard vortices will continue to affect them. Regardless, it is clear that the perturbations created by MiTEs can be used to excite a variety of vortex instabilities.

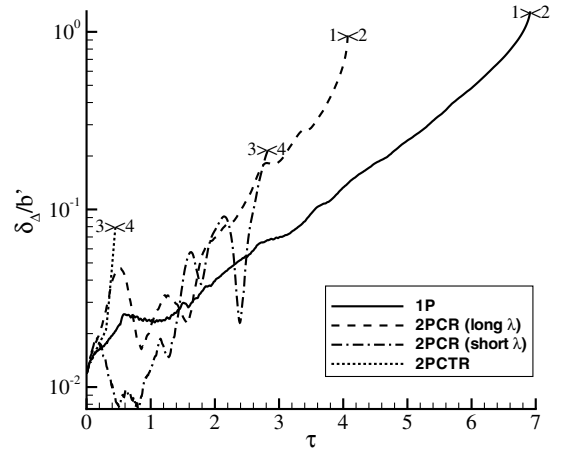

Fig. 18 Time evolution of the nondimensional displacement measure of one outboard vortex for all cases.

VI. Conclusions

The experiments and complementary computations show that MiTEs can be used to excite vortex instability and suggest that these devices can provide a solution for the wake vortex hazard. The MiTEs used in these experiments were originally intended to examine a wide parameter space and were not designed specifically for the active schemes shown here. There are likely many ways to optimize the performance of MiTEs given the actual wing loading distribution, the specific aerodynamic characteristics of the airfoil, and the particular instability to be excited.

The amplitude of perturbations created by these MiTEs are on the order of 1% of the vortex spanwise separation and are likely too small to allow pure Crow instability on one vortex pair to occur within a short enough time to effect any reduction of aircraft spacing rules. However, improvement is seen when the MiTE perturbations are used to excite instabilities on four vortex configurations. The MiTE perturbations seem capable of exciting a variety of instabilities of both long and short wavelengths. The fastest-growing instability that the MiTEs are able to excite has an initial amplification rate roughly seven times greater than that of pure Crow instability. Unfortunately, when this instability is excited by MiTE perturbations, the inboard vortices link before the outboard vortices do because of shorter wavelengths present in the MiTE perturbation. Further work would be required to determine how this inboard vortex linking affects the eventual outboard vortex linking, but this result highlights the importance of the shape of perturbations used to excite vortex instability.

Acknowledgments

This work was performed with support from the Stanford Graduate Fellowship and the Stanford University Thermal and Fluid Sciences Affiliates Program. We would also like to acknowledge Steven Rennich and Sanjiva Lele for their assistance and for providing the computational software used in this work.

References

[1] Spalart, P. R., "Airplane Trailing Vortices," *Annual Review of Fluid Mechanics*, Vol. 30, 1998, pp. 107–138.

[2] Rossow, V. J., "Lift-Generated Vortex Wakes of Subsonic Transport Aircraft," *Progress in Aerospace Sciences*, Vol. 35, No. 6, 1999, pp. 507–660.

[3] Crow, S. C., "Stability Theory for a Pair of Trailing Vortices," *AIAA Journal*, Vol. 8, No. 12, 1970, pp. 2172–2179.

[4] Crow, S. C., and Bate, E. R., Jr., "Lifespan of Trailing Vortices in a Turbulent Atmosphere," *Journal of Aircraft*, Vol. 13, No. 7, 1976, pp. 476–482.

[5] Bilanin, A. J., and Widnall, S. E., "Aircraft Wake Dissipation by Sinusoidal Instability and Vortex Breakdown," AIAA Paper 1973-107, 1973.

[6] Barber, M. R., and Tymczyszyn, J. J., "Wake Vortex Attenuation Flight

Tests: A Status Report," NASA CP-2170, 1980.
[7] Fabre, D., Jacquin, L., and Loof, A., "Optimal Perturbations in a Four-Vortex Aircraft Wake in Counter-Rotating Configuration," *Journal of Fluid Mechanics*, Vol. 451, No. 1, 2002, pp. 319–328.
[8] Fabre, D., and Jacquin, L., "Stability of a Four-Vortex Aircraft Wake Model," *Physics of Fluids*, Vol. 12, No. 10, 2000, pp. 2438–2443.
[9] Crouch, J. D., Miller, G. D., and Spalart, P. R., "Active-Control System for Breakup of Airplane Trailing Vortices," *AIAA Journal*, Vol. 39, No. 12, 2001, pp. 2374–2381.
[10] Rennich, S. C., and Lele, S. K., "Method for Accelerating the Destruction of Aircraft Wake Vortices," *Journal of Aircraft*, Vol. 36, No. 2, 1999, pp. 398–404.
[11] Rennich, S. C., "Accelerated Destruction of Aircraft Wake Vortices," Ph.D. Thesis, Stanford Univ., Stanford, CA, 1997.
[12] Crouch, J. D., "Instability and Transient Growth for Two Trailing-Vortex Pairs," *Journal of Fluid Mechanics*, Vol. 350, No. 1, 1997, pp. 311–330.
[13] Liebeck, R. H., "Design of Subsonic Airfoils for High Lift," *Journal of Aircraft*, Vol. 15, No. 9, 1978, pp. 547–561.
[14] Neuhart, D. H., and Pendergraft, O. C., Jr.,, "A Water Tunnel Study of Gurney Flaps," NASA TM-4071, 1988.
[15] Storms, B. L., and Jang, C. S., "Lift Enhancement of an Airfoil Using a Gurney Flap and Vortex Generators," *Journal of Aircraft*, Vol. 31, No. 3, 1994, pp. 542–547.
[16] Gigúere, P., Lemay, J., and Dumas, G., "Gurney Flap Effects and Scaling for Low Speed Airfoils," AIAA Paper 1995-1881, 1995.
[17] Myose, R., Heron, I., and Papadakis, M., "Effect of Gurney Flaps on a NACA 0011 Airfoil," AIAA Paper 1996-0059, 1996.
[18] Jeffrey, D. R. M., and Hurst, D. W., "Aerodynamics of the Gurney Flap," AIAA Paper 1996-2418, 1996.
[19] Myose, R., Papadakis, M., and Heron, I., "Gurney Flap Experiments on Airfoils, Wings, and Reflection Plane Model," *Journal of Aircraft*, Vol. 35, No. 2, 1998, pp. 206–211.
[20] Van Dam, C. P., and Yen, D. T., "Gurney Flap Experiments on Airfoils and Wings," *Journal of Aircraft*, Vol. 36, No. 2, 1999, pp. 484–486.
[21] Solovitz, S. A., and Eaton, J. K., "Spanwise Response Variation for Partial-Span Gurney-Type Flaps," *AIAA Journal*, Vol. 42, No. 8, 2004, pp. 1640–1643.
[22] Matalanis, C. G., and Eaton, J. K., "Wake Vortex Control Using Static Segmented Gurney Flaps," *AIAA Journal*, Vol. 45, No. 2, 2007, pp. 321–328.
[23] Spreiter, J. R., and Sacks, A. H., "The Rolling Up of the Trailing Vortex Sheet and Its Effect on the Downwash Behind Wings," *Journal of the Aeronautical Sciences*, Vol. 18, No. 1, Jan. 1951, pp. 21–32.
[24] Leonard, A., "Vortex Methods for Flow Simulation," *Journal of Computational Physics*, Vol. 37, Oct. 1980, pp. 289–335.
[25] Leonard, A., "Computing Three-Dimensional Incompressible Flows with Vortex Elements," *Annual Review of Fluid Mechanics*, Vol. 17, 1985, pp. 523–559.
[26] Widnall, S. E., "The Structure and Dynamics of Vortex Filaments," *Annual Review of Fluid Mechanics*, Vol. 7, 1975, pp. 141–165.
[27] Solovitz, S. A., and Eaton, J. K., "Dynamic Flow Response Due to Motion of Partial-Span Gurney-Type Flaps," *AIAA Journal*, Vol. 42, No. 9, 2004, pp. 1729–1736.

W. Ng
Associate Editor